

1                   **Sub-Lithospheric Small-Scale Convection Tomographically Imaged Beneath**  
2                   **the Pacific Plate**

3  
4 **Zachary C. Eilon<sup>1</sup>, Lun Zhang<sup>1</sup>, James B. Gaherty<sup>2</sup>, Donald W. Forsyth<sup>3</sup>, and Joshua B.**  
5 **Russell<sup>3</sup>**

6 <sup>1</sup> University of California Santa Barbara, Santa Barbara, CA

7 <sup>2</sup> Northern Arizona University, Flagstaff, AZ

8 <sup>3</sup> Brown University, Providence, RI

9  
10 Corresponding author: Zachary Eilon ([eilon@ucsb.edu](mailto:eilon@ucsb.edu))

11  
12 **Key Points:**

- 13       • A broadband OBS array in the equatorial Pacific allows P-wave imaging of the  
14       uppermost mantle in a region of elongated gravity anomalies
- 15       • We observe elongated P-wave velocity anomalies of order  $\pm 2\%$  beneath the oceanic  
16       lithosphere, striking parallel to gravity lineations
- 17       • These anomalies are inferred to arise from small scale convective cells beneath the plate  
18       with planform parallel to absolute plate motion

19  
20 **Key words:**

21 Oceanic lithosphere

22 Asthenosphere

23 Mantle convection

24 Body wave tomography

25 Ocean Bottom Seismometer

26 **Abstract**

27 Small-scale convection beneath the oceanic plates has been invoked to explain off-axis non-  
28 plume volcanism, departure from simple seafloor depth-age relationships, and intraplate gravity  
29 lineations. We deployed thirty broadband OBS stations on ~40 Ma seafloor in the equatorial  
30 Pacific, in a region notable for gravity anomalies measured by satellite altimetry elongated in the  
31 direction of plate motion. P-wave teleseismic tomography reveals alternating upper mantle  
32 velocity anomalies on the order of  $\pm 2\%$ , oriented parallel to the gravity lineations. These  
33 features, which correspond to ~300-500 °K lateral temperature contrast, and possible hydrous or  
34 carbonatitic partial melt, are strongest between 150 and 260 km depth, indicating rapid vertical  
35 motions through a low-viscosity asthenospheric channel. Coherence and admittance analysis  
36 using new multibeam bathymetry soundings substantiates the presence of asthenospheric density  
37 variation, and forward modelling predicts gravity anomalies that qualitatively match observed  
38 lineations. This study provides observational support for small-scale convective rolls beneath the  
39 oceanic plates.

40

41 **Plain Language Summary**

42 Covered by kilometers of water, and therefore hard to access, Earth's oceanic tectonic plates  
43 have several features we cannot explain. Among these are linear undulations ("rolls") in the  
44 strength of gravity at the sea surface. Using data from a rare underwater seismic experiment, we  
45 have produced 3-D maps of seismic properties of Earth's sub-surface in a location of clear  
46 gravity rolls. We find linear blobs of fast and slow material in the mantle beneath the oceanic  
47 plate, parallel to the gravity features. These represent cold sinking and warmer rising material,  
48 revealing a highly dynamic convective system underneath the plate which has long been  
49 theorized but not previously directly observed at this scale.

50

## 51 **1. Introduction**

52

53

54

55

56

57

58

59

60

61

62

63

64

65

66

67

68

69

70

71

72

73

74

75

76

77

78

79

80

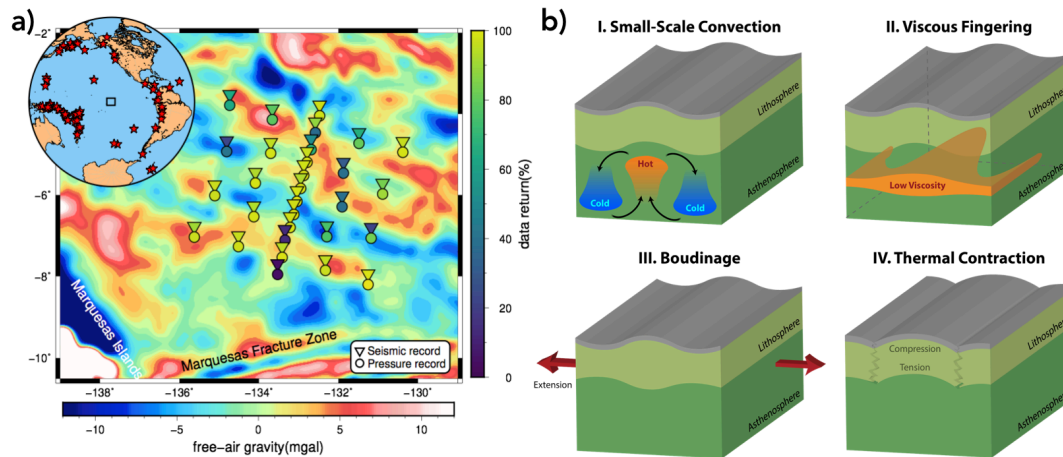
81

82

Traditional plate tectonic models fail to explain several aspects of the oceanic lithosphere. For instance, widespread off-axis, non-plume volcanism within the Pacific plate has unknown origin (Ballmer et al., 2009; D. T. Sandwell et al., 1995), while the depth-age relationship predicted by lithospheric conductive cooling models breaks down in old (>70 Ma) ocean plates with anomalously shallow seafloor topography and high heat flow (Crosby et al., 2006; Parsons & Sclater, 1977; Parsons & McKenzie, 1978; Stein & Stein, 1992). Sub-lithospheric small scale convection (SSC) (Ballmer et al., 2007; Buck, 1985; Haxby & Weissel, 1986) has been proposed to explain these phenomena. This dynamic process, which is favored by a thicker, lower-viscosity asthenospheric layer, would increase the heat flow at the base of the lithospheric thermal boundary layer, and could concentrate upwellings and consequent melting. SSC spontaneously develops in the upper mantle due to the instabilities at the base of lithosphere whenever its thickness exceeds a critical value (Ballmer et al., 2007; Buck & Parmentier, 1986). It is expected to take the form of convective rolls aligned with absolute plate motion (APM) (Buck & Parmentier, 1986; Richter & Parsons, 1975) (Fig. 1b) due to shear between the plate and the deeper mantle. Despite the geodynamic significance of SSC beneath the oceanic plates, it has never previously been directly imaged at length scales  $< \sim 2000$  km (French et al., 2013) with seismic tomography beneath mature oceanic plate.

To date, the most powerful argument for widespread SSC beneath the plates are free air gravity lineations observed in the oceans, aligned parallel to APM and with wavelength of  $\sim 150$ -400 km, comparable to SSC predictions (Haxby & Weissel, 1986). Others have proposed alternative explanations for these gravity anomalies, including mechanical modification of the lithosphere and viscous fingering (Bull et al., 1992; Cormier et al., 2011; Gans et al., 2003; Sandwell & Fialko, 2004; Sandwell et al., 1995). Lithospheric boudinage (non-linear lithospheric extension) or thermal contraction bending (Fig. 1b) can produce elongated topographic and gravity undulations. Associated cracking might provide conduits for upward percolation of preexisting asthenospheric melt to form volcanic ridges; in this case the drainage of melt might lead to shallow high-velocity anomalies beneath the ridges (Karato & Jung, 1998). Viscous fingering, caused by lateral intrusion of low-viscosity material within a thin asthenospheric channel (Fig. 1b) has also been proposed to explain spreading-aligned ridge-adjacent seamounts, gravity variation, and long-wavelength

83 velocity anomalies beneath young seafloor (Holmes et al., 2007; Weeraratne et al., 2007). Our  
 84 study area is in older seafloor in a region with no volcanic ridges or major seamounts. Notably,  
 85 gravity lineations here obliquely cross fracture zones (that record fossilized relative plate motion),  
 86 suggesting they are not inherited from the mid-ocean ridges.



87

88

89 **Fig. 1 | Map of the research area (a) and schematics of candidate processes causing gravity**  
 90 **lineations (b).** *a*, Broadband OBS array comprising three-component seismometers (triangles)  
 91 with differential pressure gauge (circles). Symbol colors indicate fractional data return, and the  
 92 underlying map shows filtered free air gravity anomalies (Figure S9). Inset shows location of the  
 93 array, with stars representing earthquakes from which differential travel times were measured. *b*,  
 94 Block diagrams showing exaggerated lithospheric and asthenospheric structures proposed to  
 95 explain free air gravity undulations (adapted after Weeraratne et al., 2007). Any bathymetric  
 96 anomalies, exaggerated here, are highly contingent on elastic thickness of the lithosphere.

97

98 Discriminating the above hypotheses requires tomographic resolution of features with <200  
 99 km lateral wavelength in the upper mantle, together with high-precision local constraints on  
 100 bathymetry. Sparse island stations and ocean basin-traversing seismic rays offer only coarse  
 101 imaging of the oceanic upper mantle. A previous study, the GLIMPSE Ocean Bottom Seismometer  
 102 (OBS) experiment (Forsyth et al., 2006) aimed to probe gravity lineations in ~2-10 Ma Pacific  
 103 plate just west of the East Pacific Rise (EPR). Body (Harmon et al., 2007) and Rayleigh wave  
 104 (Weeraratne et al., 2007) imaging revealed elongate low velocity lineaments beneath volcanic  
 105 ridges with lateral wavelength of order ~250 km. Substantial data loss precluded fine depth

106 resolution with body waves, but velocity variation was estimated using surface waves to reside at  
107 <70 km depth. No other OBS experiments before or since have imaged uppermost mantle 3-D  
108 isotropic wave speed variations suggestive of small scale convection in regions unperturbed by  
109 plume or other intra- or inter-plate volcanic activity.

110

## 111 **2. Data**

112

113 The Pacific OBS Research into Convecting Asthenosphere (ORCA) experiment (Eilon et al.,  
114 2022) deployed 30 OBS instruments across a 500x500 km<sup>2</sup> footprint on ~40 Ma lithosphere  
115 northeast of Marquesas Islands. These instruments, deployed for 13 months, included three-  
116 component broadband seismometers and differential pressure gauges. The array was oriented  
117 approximately orthogonal to  $\pm 15$  mGal free air gravity lineations observed from Seasat altimetry  
118 (Haxby & Weissel, 1986), with aperture spanning 2-3 wavelengths (~500 km) of the gravity rolls  
119 (Fig. 1a). This experiment also collected new high-resolution multibeam swath data which has  
120 been integrated into the global seafloor database (Smith & Sandwell, 1997) to provide substantially  
121 better constrained bathymetry in this region.

122

123 We extracted the vertical seismic and pressure waveforms for P-wave arrivals recorded on the  
124 ORCA array from teleseismic events ( $>30^\circ$  distance; Fig. 1) in the GCMT catalogue between April  
125 2018 and May 2019 with moment magnitudes  $\geq 5.5$ . For each event, we measured relative arrival  
126 times of direct *P*-waves using multi-channel cross-correlation (MCCC; Fig. S1) (VanDecar &  
127 Crosson, 1990) on vertical and pressure records independently, yielding 1096 and 598 differential  
128 travel times respectively. We combined these data (see *Supporting Information*) to yield 1196 high-  
129 quality P-wave travel times (Supp. Fig. 2a).

130

## 131 **3. Methods**

132

133 We inverted these differential travel times for 3-D upper mantle *P*-wave velocity perturbations  
134 ( $\delta V_p$ ) using a finite frequency tomography approach. To regularize the inverse problem we applied  
135 both model norm damping and first derivative damping (*i.e.*, “flattening”) with a horizontal-to-  
136 vertical smoothing ratio of 2. We weighted observations by estimating travel time errors *a*

137 *posteriori* during the MCCC process. To avoid unrealistically low estimated errors, we set a  
138 minimum standard deviation of 0.625s, equal to 1/20 of the central filter period. We solved for  
139 station and event static terms. Optimal regularization parameter values were determined by L-test.  
140 For a much more comprehensive description of the inverse problem, see the *Supporting*  
141 *Information*.

142

143 To explore apparent lineations in observed velocity structure, we conducted a series of “2.5-  
144 D” inversions by enforcing flattening (*i.e.*, no model variation) along a single horizontal direction,  
145 seeking a lineation direction that minimized data misfit. We also evaluated the resolution and  
146 reliability of our inversion through input-output tests that included checkerboard structures (Fig.  
147 S5) and velocity lineations that mimic features of dynamical interest (Fig. S4). For checkerboard  
148 tests, we quantify feature recovery using semblance (Zelt, 1998) computed at each point over a 3-  
149 D volume with radius equal to checker length scale. Finally, we performed a suite of inversions  
150 for which the model nodes below and above various “squeezing depths” were heavily damped. By  
151 evaluating the fractional reduction in overall data fit for each squeezed case, and observing whether  
152 or not the inversion re-injects structure once the damping is relaxed (see *Supporting Information*),  
153 we determined the depth range over which the data require major velocity anomalies.

154

## 155 **4. Results**

156

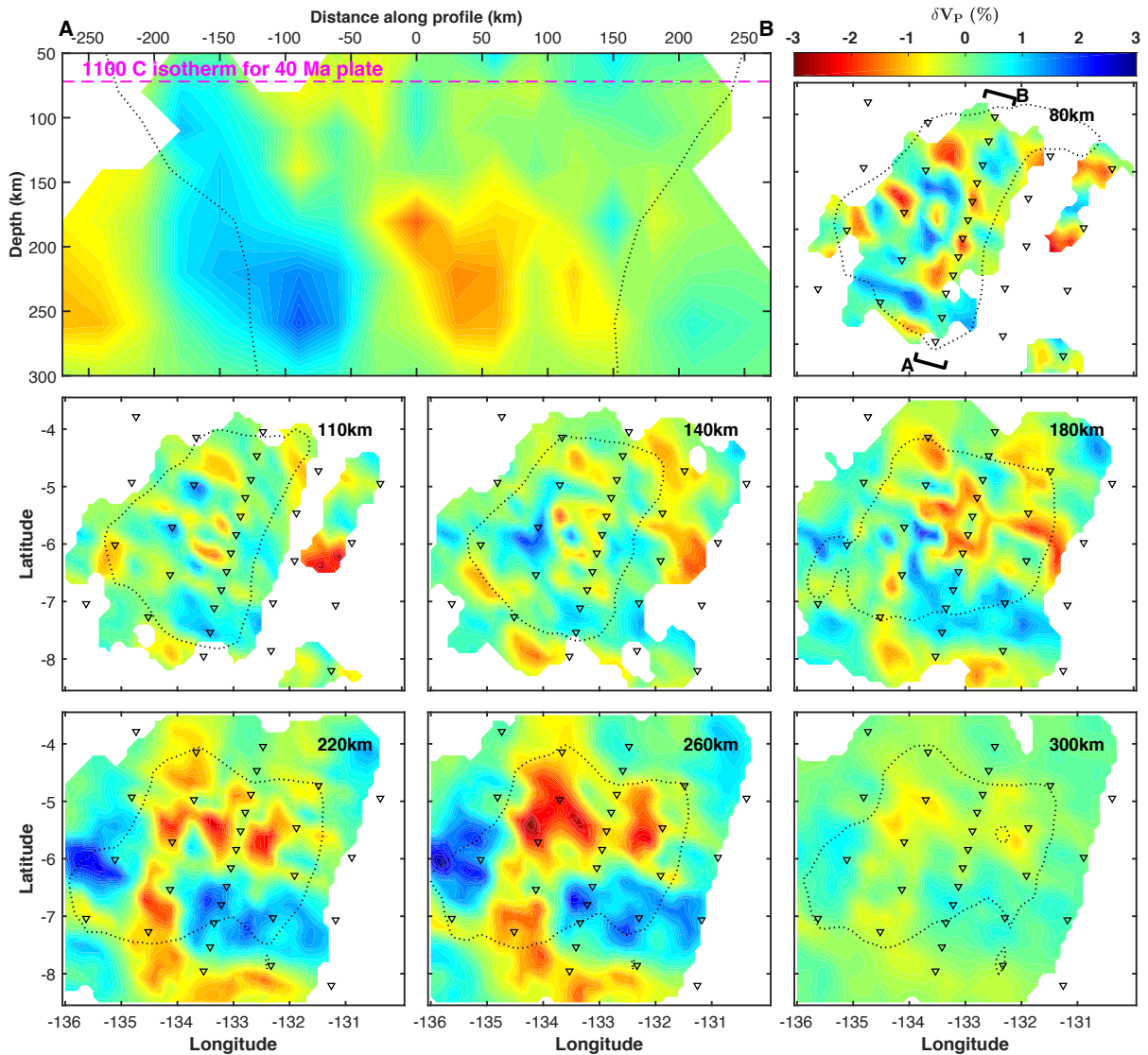
### 157 **4.1 Tomographic inversion**

158 Simple thermal cooling models predict essentially no upper mantle velocity heterogeneity on the  
159 length scale of this array. Nonetheless, we measured differential arrival times of up to  $\pm 0.5$ s (with  
160 an RMS of 0.27 s). This travel time variance substantially exceeds signal that can be produced in  
161 the crust, and systematic back azimuthal variations seen at several stations confirm this signal to  
162 have an upper mantle origin (Figure S2).

163

164 Our tomographic model shows substantial upper-mantle velocity structure. The most prominent  
165 pattern in the 3D model (Fig. 2) is alternating velocity anomaly bands parallel to local gravity  
166 lineations, with lateral wavelength  $\sim 250$ -300 km. The amplitude of these anomalies is on the order  
167 of  $\pm 2\%$  ( $\pm 2.3\%$  for the 1-99 percentiles, or  $\pm 1.8\%$  for the 2.5-97.5 percentiles, in the best resolved

168 regions; Fig. S8). For our preferred model, the final RMS data error was 0.23s, the RMS of event  
 169 static values was 0.10 s and the RMS of station static values was 0.01 s. The weighted variance  
 170 reduction was 85.29%, indicating good data fit.



171

172

173 **Fig. 2 | The tomographic model.** A vertical slice (top left) and several horizontal slices through  
 174 our preferred 3-D  $\delta V_p$  model, where structure is shown only for model nodes with ‘hit quality’  
 175 (Eilon et al., 2015) above 0.3. Black dotted line shows region with semblance (a measure of  
 176 checkerboard recovery (Zelt, 1998)) greater than 0.7. The vertical section depicts values  
 177 averaged  $\pm 30$  km in the direction perpendicular to the line of the section (indicated by black  
 178 brackets in the 80 km depth cross-section), to avoid overly emphasizing any particular plane.

179

**180 4.2 Testing the model**

181 2.5-D inversions to test for preferred lineation (Figs. 3, S7) showed that best fit to data (78%  
182 as good as the full 3-D model) involves structure elongated in the 115° direction (Fig. 3b). We  
183 infer that this direction reflects the dominant structural elongation. This orientation is subparallel  
184 to (independently constrained) gravity lineations and local absolute plate motion. Note, this  
185 minimum-misfit 2.5-D model (Fig. 3b) was used to compute 1-D gravity variations (Fig. 4).

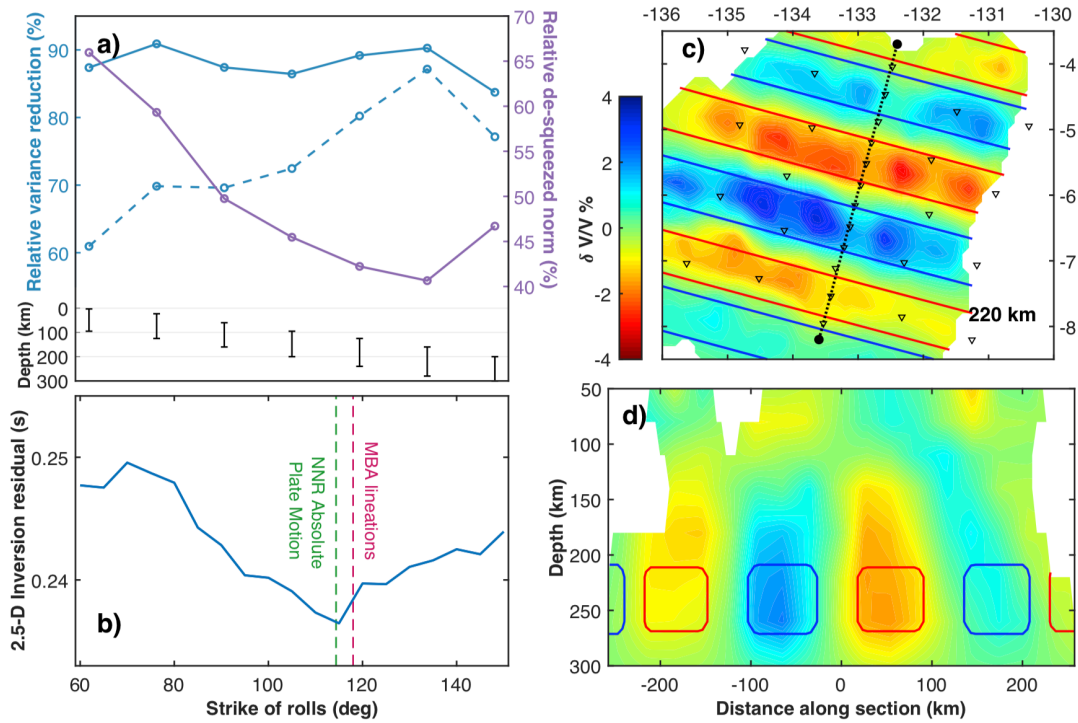
186

187 Synthetic tests indicated that our data coverage can indeed recover the geometry and position of  
188 the observed features (Fig. 3, S4, S5). These tests – especially at the model edges – suffer from as  
189 much as 40% amplitude loss due to sparse seismic ray coverage. This observation, typical for these  
190 sorts of regularized inversions, theoretically implies that observed velocity, and hence inferred  
191 temperature, contrasts are in fact lower bounds.

192

193 We individually tested shallow squeezing and deep squeezing, finding that the data require  
194 relatively deep anomalies: at least 140km, and as much as 300 km in depth (Figs. S4, S6). We  
195 attempted to quantitatively determine the optimal depth range for the most prominent mantle  
196 velocity anomalies by squeezing structure into a moving window of three model layers (Fig. 3).  
197 These tests showed that the data require the most prominent anomalies to be fit by structure within  
198 the 180-260km depth range. This finding is not particular to a three-layer test; similar two- and  
199 four-layer tests confirmed that the 140-260 km depths are most important to fitting the data. This  
200 finding does not preclude structure at other depths in the model, rather it indicates that velocity  
201 anomalies in this depth range have the greatest influence on measured travel times. Lastly, we  
202 explored the depth extent of imaged features by increasing the model base to 480 km (Fig. S6).  
203 We found that although some structure is smeared to depths >300 km, the pattern of the anomalies  
204 is extremely similar to the preferred model, and the strongest anomalies are still present in the 150-  
205 300 km depth range.

206



207

208

209 **Fig. 3 | Tests of the tomographic model.** *a)* Squeezing tests of anomaly depth. Lower subplot shows  
 210 depth extent over which structure was allowed to enter into the model space, while upper subplot  
 211 shows data fit (measured by variance reduction – high values indicate better data fit) and  
 212 explanatory power of the un-squeezed region of model space (purple line; low values indicate the  
 213 squeezed model does a better job of explaining the data) for the associated models. Variance  
 214 reduction is plotted relative to the un-damped, preferred, model. De-squeezed model norm is  
 215 plotted relative to the norm of the squeezed model in each iteration and can thus be thought of as  
 216 fractional model addition once squeezing is relaxed. *b)* Tests of feature elongation direction,  
 217 showing data misfit (residual) when grid searching through possible orientations of 2.5-D models.  
 218 *c)* Horizontal slice and *d)* vertical section through models yielded by synthetic recovery tests with  
 219 input rectangular velocity anomalies (dashed lines) of  $\pm 4\%$ .

220

### 221 4.3 Gravity signals

222 The ORCA experiment measured high-resolution multibeam topography throughout the OBS  
 223 array footprint, allowing for detailed comparison with gravity (Fig. S9). To identify subsurface  
 224 density heterogeneity, we computed free air coherence and admittance, and the theoretical mantle  
 225 Bouguer anomaly (MBA; see *Supporting Information*). At wavelengths greater than 20 km,

226 observed free air admittance in this region is approximately 0.025 mGal/m. This value is  
227 substantially less than the theoretical admittance for uncompensated topography, but also  
228 significantly greater than the prediction for topography compensated at the Moho (Fig. S10).

229

## 230 **5. Discussion and conclusions**

231

### 232 **5.1 Thermal anomalies**

233 The tomographic models show alternating slow and fast  $\delta V_p$  features within the oceanic  
234 asthenosphere. We infer that these features result from hot upwellings and cold downwellings,  
235 respectively. These cells take the approximate form of cylindrical rolls, with horizontal length  
236 scale  $\sim 250$ - $300$  km and aspect ratio approximately unity. These features are not consistent with  
237 lithospheric warping (boudinage or cracking), which predict negligible, and certainly not  $>200$  km  
238 deep, upper-mantle velocity variations. They are also not consistent with viscous fingering, which  
239 would require velocity variations confined to a shallow ( $<100$  km deep) and thin ( $<30$  km thick)  
240 channel (Weeraratne & Parmentier, pers. comm.) Rather, these observations provide the first  
241 tomographic evidence for small-length-scale thermal convection beneath the oceanic plates,  
242 aligned by shear between the plate and underlying deeper mantle.

243

244 Differential travel time tomography provides constraints only on lateral velocity gradients, not  
245 absolute velocity. The  $\sim 4\%$  peak-to-peak amplitude of the observed velocity anomalies is  
246 relatively high. Absent melt, this implies up to  $\sim 500^\circ\text{C}$  lateral temperature variations (see  
247 *Supporting Information*; Fig. S8). Our default expectation is that SSC is driven here by positive  
248 density anomalies that drip or sink from the base of the lithospheric thermal boundary layer. In  
249 this framework, the fast  $dV_p$  anomalies correspond to material that is cold in an absolute sense,  
250 while the slow  $dV_p$  anomalies represent relatively warm ambient mantle.

251

252 However, upwelling parcels displaced by the downwellings must undergo adiabatic  
253 decompression. If the mantle contains dissolved volatiles, this upwelling material could produce  
254 small-fraction hydrous and/or carbonatitic melt fraction even at depths up to 200 km (Dasgupta et  
255 al., 2013; Hirschmann, 2010). Melting could introduce a small active component to upwellings by  
256 reducing density and viscosity. Melt would also lower the absolute P-wave velocity in the

257 upwelling cells. Accounting for both elastic and anelastic effects (see *Supporting Information*), the  
258 observed peak-to-peak  $dVp$  variation can also be explained by a 0.5% melt fraction, together with  
259 a  $dT$  of  $\sim 300^\circ\text{C}$  (Fig. S8). We prefer this latter (temperature plus melt) scenario for explaining  
260 observed anomalies, since the implied temperature gradient is more consistent with (although still  
261 greater than) the temperature contrast invoked in numerical models of sub-lithospheric SSC  
262 (Ballmer et al., 2009; Manjón-Cabeza Córdoba & Ballmer, 2021). This same analysis predicts a  
263  $Q_\mu$  of 100-180 in the oceanic asthenosphere, consistent with previous observations (Ma et al.,  
264 2020).

265

## 266 **5.2 Gravity analysis and modelling**

267 A closer examination of observed gravity anomalies provides further insight. Free air  
268 admittance indicates some degree of isostatic compensation here. Remaining support for  
269 bathymetry must come from plate strength, in line with previous  $>15$  km estimates of effective  
270 elastic thickness here (Fischer et al., 1986).

271

272 The observed compensation must result from some combination of crustal thickness variations  
273 and upper mantle density anomalies. Three primary observations suggest a substantial influence  
274 from the upper mantle. Firstly, MBA anomalies here (striking  $\sim 120^\circ$ ) are oriented sub-parallel to  
275 plate motion ( $\sim 115^\circ$ ), rather than the paleo-spreading direction inferred from abyssal hill fabric  
276 and nearby fracture zones ( $\sim 75^\circ$ , although we do note a due E-W swath of seafloor in this region  
277 with  $\sim 105^\circ$  apparent spreading direction indicated by the trend of the abyssal hill topography (Eilon  
278 et al., 2022), perhaps due to oblique spreading, a ridge jump or large overlapping spreading center).  
279 Secondly, if the observed gravity and bathymetry anomalies were created from a single mechanism  
280 then the coherence should be unity. We observe coherence lower than 0.7 associated with the  
281 longest-wavelengths (Fig. S10). Finally, the predicted free air anomaly for compensation at Moho  
282 depths under-predicts the admittance, requiring either deeper compensation or density anomalies  
283 beneath an elastic plate with flexural rigidity that dampens the topographic expression. Our  
284 inference is that multiple mechanisms are at play here, pointing to the loading of a finite-rigidity  
285 plate from below as a result of density variations in the mantle, in addition to “frozen-in” partial  
286 compensation of the topographic relief by variations in crustal thickness.

287

288 As a proof-of-concept, we explored the correspondence between the MBA and our velocity model.  
289 For simplicity, and given the strongly linear features in both models, we collapsed the MBA to 1.5  
290 dimensions (*i.e.*, varying in the roll-perpendicular-direction but homogenous in the roll-parallel-  
291 direction), using a log-spaced sinusoidal basis. The best fit 1.5-D gravity field (explaining 28% of  
292 the full 2-D signal) comprises lineations aligned  $118^\circ$  from North. We compare this gravity  
293 anomaly to the 2.5-D velocity model smoothed in the same direction, considering  $dV_p$  variations  
294 only in the plane defined by the vertical and the direction perpendicular to the gravity rolls (Fig.  
295 4). There is no direct association between the pattern of deep (200-300 km)  $dV_p$  anomalies and the  
296 residual gravity, other than similarity in their wavelength (225-300 km) of variation and orientation  
297 of the lineations. This is not surprising: periodic density anomalies at depth approximately equal  
298 to their wavelength should negligibly affect surface gravity due to upward continuation. However,  
299 using our 2.5-D tomography model to forward calculate 1.5-D gravity variations (see *Supporting*  
300 *Information*, and note this calculation used the more modest temperature variation outlined above,  
301 adding support to that scenario), we found good qualitative match between observed and predicted  
302 signal, where the predicted signal is dominated by the shallowest features in the velocity model  
303 (Fig. 4). Although this portion of the model is not as well resolved, the agreement is striking and  
304 demonstrates that mantle temperature heterogeneity alone can theoretically explain the MBA  
305 gravity anomaly.

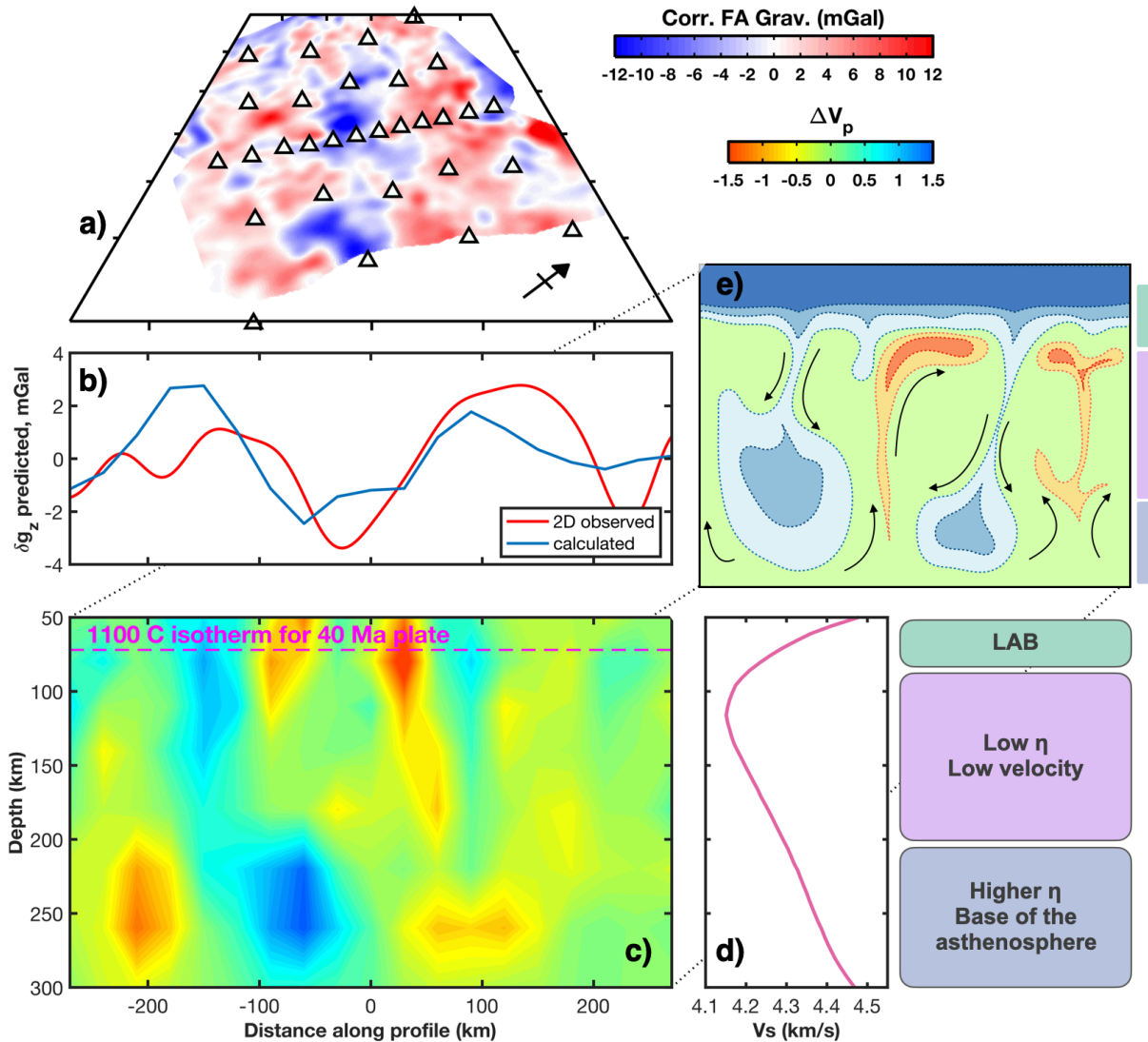
306

### 307 **5.3 Asthenospheric rheology**

308

309 The depth, vertical extent, and wavelength of putative convective features imaged in this study  
310 connect to the rheology of the asthenosphere. The presumed source of convective instability, is  
311 near the base of the plate. For 40 Ma oceans (assuming mantle potential temperature,  $T_m$ , of  
312  $1350^\circ\text{C}$  and thermal diffusivity of  $10^{-6} \text{ m}^2/\text{s}$ ), the depth to the  $1150^\circ\text{C}$  isotherm (the  $0.85 T_m$  value  
313 often used to approximate the thermal lithosphere-asthenosphere boundary) is 73 km. The  
314 agreement between the strike of the rolls and local APM in a no-net rotation reference frame  
315 (DeMets et al., 2010), together with the lack of another obvious alternative source for small-scale  
316 lateral thermal gradients, argues that these features are not deep-rooted but derive from convective  
317 processes near the bottom of the plate. Station spacing limits our resolution shallower than  $\sim 50$   
318 km, but synthetic recovery tests indicate that we should have imaged large-scale velocity

319 anomalies in the 100-200 km depth range, if they were present (Figs. S4, S5). It is surprising, then,  
 320 that the strongest velocity features in the model are as deep as 250 km and that squeezing tests  
 321 suggest that the strongest anomalies are deeper than 200 km (Fig. 3).  
 322



323  
 324

325 **Fig. 4 | Dynamic summary and comparison between gravity and tomography.** *a)* Mantle Bouguer  
 326 gravity anomaly corrected for effects of bathymetry and filtered as in Fig. S9. *b)* One-dimensional  
 327 variation in gravity anomaly obtained from sinusoidal fitting of observed field (red) and velocity-  
 328 temperature-density forward modelling (blue) of the model depicted in panel (c). The orientation  
 329 of the section is  $\sim 30^\circ$  east of North. *c)* Cross section through the 2.5-D velocity model,

330 *perpendicular to enforced smoothing direction. d) 1-D shear velocity profile obtained from*  
331 *inversion of Rayleigh wave phase velocities averaged across ORCA array (Russell, 2021). e)*  
332 *Cartoon cross-section of small scale convection beneath the plate, where bluer colors correspond*  
333 *to colder and more dense material and redder colors correspond to hotter and less dense material.*

334

335 A comparison between Rayleigh wave imaging at young ORCA and NoMelt (70 Ma crust)  
336 indicates that the young ORCA region exhibits anomalously slow absolute shear velocity beneath  
337 the plate (Fig. 4), with a broad velocity minimum from 75-200 km depth (Russell et al., 2021).  
338 Small scale convection is favored by a wider low viscosity layer, and the middle of this layer is  
339 expected to be roughly isothermal. Our observed anomalies appear deeper than the slowest (and  
340 presumably weakest) part of the asthenosphere. It is possible that density anomalies are preserved  
341 at lithospheric levels (<100 km depth) and deeper than 200 km due to higher viscosity, while the  
342 lowest-viscosity portion of the asthenosphere is roughly isothermal and contains convective  
343 structures too fine to resolve. A similar mechanism has been suggested to explain a minimum in  
344 the strength of azimuthal anisotropy in the center of the oceanic asthenosphere observed by other  
345 focused OBS arrays (Lin et al., 2016; Russell et al., 2019).

346

347 This suite of observations suggests a sub-lithospheric SSC system wherein the gravity and  
348 velocity anomalies correspond to the upper and lower thermal boundary layers of an  
349 asthenosphere-scale convective system, respectively. We posit three depth regimes (Fig 4): 1) The  
350 base of the plate (50-100 km), the source of the density instabilities and part of the Bouguer gravity  
351 anomalies. The elastic lithosphere partially damps the effect on bathymetry. 2) The low-viscosity  
352 center of the asthenosphere (100-200 km), coinciding with the lowest velocities in a surface-wave-  
353 derived 1-D shear velocity model (Fig. 4). Imaged anomalies in this regime are minimal, despite  
354 good resolving power. We infer that once an instability develops, it sinks rapidly through the low  
355 viscosity asthenosphere (Ballmer et al., 2009), perhaps leaving behind thin convective sheets or  
356 spokes connecting regimes (1) and (3) that are too narrow to be imaged tomographically. 3) A  
357 higher viscosity base of the asthenosphere (200-300 km), where high-density anomalies encounter  
358 resistance to sinking and pile up, making for clearly imaged velocity anomalies. Ambient mantle  
359 displaced upwards at this depth begins to melt (requiring volatiles to reduce the solidus (Dasgupta

360 et al., 2013; Hirschmann, 2010)), reducing seismic velocities in the upwelling volumes between  
361 the downwelling limbs.

362 This work provides evidence for a highly dynamic asthenospheric system beneath the central  
363 oceanic plates, involving small scale lithospheric delamination, and small-fraction hydrous  
364 and/or carbonatite melt. Since intraplate volcanism is not ubiquitous in the oceans, upward  
365 pathways for melt transport through the lithosphere must be rare. Rather, this melt may pond or  
366 freeze in laminae at the base of the plate, contributing to a sharp and possibly radially anisotropic  
367 LAB structure observed widely in the Pacific (Beghein et al., 2014; Kawakatsu et al., 2009;  
368 Stern et al., 2015). In addition, SSC might introduce uneven topography on the LAB that is not a  
369 simple function of age. Together, these phenomena help explain the variability in seismic  
370 discontinuities in the uppermost (<100 km depth) oceanic mantle (Schmerr, 2012; Tharimena et  
371 al., 2017).

372 **Acknowledgments**

373 This work was funded by NSF grants OCE-1658491, OCE-1658214, OCE-1658070, and OCE-  
374 2051265. The OBS instruments were provided by the Scripps Institution of Oceanography,  
375 coordinated by the OBS Instrument Centre at the Woods Hole Oceanographic Institute. We are  
376 grateful to Dave Sandwell for sharing codes and illuminating discussions. We thank the ships'  
377 captains, crew, and research technicians, as well as the cruise science parties, who were all  
378 indispensable to collecting these data. The authors declare no conflicts of interest associated with  
379 this study.

380

381 **Open Research: Data and code availability**

382 The seismic data from this experiment are available through the Incorporated Research  
383 Institutions for Seismology's Data Management Center, under the network code XE (2018-  
384 2019). Metadata information is catalogued within Eilon et al. (2022) (DOI  
385 10.1785/0220210173). Multibeam swath bathymetry data is available via the Rolling Deck to  
386 Repository portal (DOIs 10.7284/907958 and 10.7284/908257). Free air gravity data is available  
387 at [https://topex.ucsd.edu/pub/global\\_grav\\_1min/](https://topex.ucsd.edu/pub/global_grav_1min/) and bathymetry at  
388 [https://topex.ucsd.edu/pub/global\\_topo\\_1min](https://topex.ucsd.edu/pub/global_topo_1min). Codes for all the analysis and figures above are  
389 provided via a Dryad repository [#DOI insert available after submission#].

390 **References**

- 391 Abers, G. A., & Hacker, B. R. (2016). A MATLAB toolbox and Excel workbook for calculating  
392 the densities, seismic wave speeds, and major element composition of minerals and rocks at  
393 pressure and temperature. *Geochemistry Geophysics Geosystems*, *17*(2), 616–624.  
394 <https://doi.org/10.1002/2015gc006171>
- 395 Ballmer, M. D., Hunen, J. van, & Ito, G. (2007). Non-hotspot volcano chains originating from  
396 small-scale sublithospheric convection. *Geophysical Research Letters*, *34*, L23310.  
397 <https://doi.org/10.1029/2007gl031636/pdf>
- 398 Ballmer, M. D., Hunen, J. van, Ito, G., Bianco, T. A., & Tackley, P. J. (2009). Intraplate  
399 volcanism with complex age-distance patterns: A case for small-scale sublithospheric  
400 convection. *Geochemistry Geophysics Geosystems*, *10*(6), n/a-n/a.
- 401 Bechtel, T. D., Forsyth, D. W., & Swain, C. J. (1987). Mechanisms of isostatic compensation in  
402 the vicinity of the East African Rift, Kenya. *Geophysical Journal International*, *90*(2), 445–  
403 465. <https://doi.org/10.1111/j.1365-246X.1987.tb00734.x>
- 404 Beghein, C., Yuan, K., Schmerr, N., & Xing, Z. (2014). Changes in Seismic Anisotropy Shed  
405 Light on the Nature of the Gutenberg Discontinuity. *Science*, *343*(6176), 1237–1240.  
406 <https://doi.org/10.1126/science.1246724>
- 407 Behn, M. D., Hirth, G., & II, J. R. E. (2009). Implications of grain size evolution on the seismic  
408 structure of the oceanic upper mantle. *Earth and Planetary Science Letters*, *282*(1–4), 178–  
409 189. <https://doi.org/10.1016/j.epsl.2009.03.014>
- 410 Brunsvik, B. R., Eilon, Z. C., & Lynner, C. (2021). Mantle Structure and Flow Across the  
411 Continent-Ocean Transition of the Eastern North American Margin: Anisotropic *S*-Wave

- 412 Tomography. *Geochemistry, Geophysics, Geosystems*, 22(12).  
413 <https://doi.org/10.1029/2021GC010084>
- 414 Buck, W. R. (1985). When does small-scale convection begin beneath oceanic lithosphere?  
415 *Nature*, 313(6005), 775–777. <https://doi.org/10.1038/313775a0>
- 416 Buck, W. R., & Parmentier, E. M. (1986). Convection beneath young oceanic lithosphere:  
417 Implications for thermal structure and gravity. *Journal of Geophysical Research-Solid Earth*  
418 *and Planets*, 91(B2), 1961–1974. <https://doi.org/10.1029/jb091ib02p01961>
- 419 Bull, J. M., Martinod, J., & Davy, P. (1992). Buckling of the oceanic lithosphere from  
420 geophysical data and experiments. *Tectonics*, 11(3), 537–548.  
421 <https://doi.org/10.1029/91TC02908>
- 422 Cormier, M.-H., Gans, K. D., & Wilson, D. S. (2011). Gravity lineaments of the Cocos Plate:  
423 Evidence for a thermal contraction crack origin. *Geochemistry Geophysics Geosystems*, 12(7),  
424 n/a-n/a. <https://doi.org/10.1029/2011gc003573>
- 425 Crosby, A. G., McKenzie, D., & Sclater, J. G. (2006). The relationship between depth, age and  
426 gravity in the oceans. *Geophysical Journal International*, 166(2), 553–573.  
427 <https://doi.org/10.1111/j.1365-246x.2006.03015.x>
- 428 Dasgupta, R., Mallik, A., Tsuno, K., Withers, A. C., & Hirth, G. (2013). Carbon-dioxide-rich  
429 silicate melt in the Earth's upper mantle. *Nature*, 493(7431), 211–215.  
430 <https://doi.org/10.1038/nature11731>
- 431 DeMets, C., Gordon, R. G., & Argus, D. F. (2010). Geologically current plate motions.  
432 *Geophysical Journal*, 181, 1–80.

- 433 Eilon, Z., Abers, G. A., Gaherty, J. B., & Jin, G. (2015). Imaging continental breakup using  
434 teleseismic body waves: The Woodlark Rift, Papua New Guinea. *Geochemistry, Geophysics,*  
435 *Geosystems*, 16(8), 2529–2548. <https://doi.org/10.1002/2015GC005835>
- 436 Eilon, Z. C., & Abers, G. A. (2017). High seismic attenuation at a mid-ocean ridge reveals the  
437 distribution of deep melt. *Science Advances*, 3(5), e1602829.  
438 <https://doi.org/10.1126/sciadv.1602829>
- 439 Eilon, Z. C., Gaherty, J. B., Zhang, L., Russell, J., McPeak, S., Phillips, J., et al. (2022). The  
440 Pacific OBS Research into Convecting Asthenosphere (ORCA) Experiment. *Seismological*  
441 *Research Letters*, 93(1), 477–493. <https://doi.org/10.1785/0220210173>
- 442 Fischer, K. M., McNutt, M. K., & Shure, L. (1986). Thermal and mechanical constraints on the  
443 lithosphere beneath the Marquesas swell. *Nature*, 322(6081), 733–736.  
444 <https://doi.org/10.1038/322733a0>
- 445 Forsyth, D. W., Harmon, N., Scheirer, D. S., & Duncan, R. A. (2006). Distribution of recent  
446 volcanism and the morphology of seamounts and ridges in the GLIMPSE study area:  
447 Implications for the lithospheric cracking hypothesis for the origin of intraplate, non-hot spot  
448 volcanic chains. *Journal of Geophysical Research*, 111(B11), n/a-n/a.  
449 <https://doi.org/10.1029/2005jb004075>
- 450 French, S., Lekic, V., & Romanowicz, B. (2013). Waveform tomography reveals channeled flow  
451 at the base of the oceanic asthenosphere. *Science*, 342(6155), 224–227.  
452 <https://doi.org/10.1126/science.1242248>
- 453 Gans, K. D., Wilson, D. S., & Macdonald, K. C. (2003). Pacific Plate gravity lineaments: Diffuse  
454 extension or thermal contraction? *Geochemistry, Geophysics, Geosystems*, 4(9), 1074.  
455 <https://doi.org/10.1029/2002GC000465>

- 456 Garcia, E. S., Sandwell, D. T., & Smith, W. H. F. (2014). Retracking CryoSat-2, Envisat and  
457 Jason-1 radar altimetry waveforms for improved gravity field recovery. *Geophysical Journal*  
458 *International*, 196(3), 1402–1422. <https://doi.org/10.1093/gji/ggt469>
- 459 Hammond, W. C., & Humphreys, E. D. (2000). Upper mantle seismic wave velocity: Effects of  
460 realistic partial melt geometries. *Journal of Geophysical Research*, 105(B5), 10975–10986.  
461 <https://doi.org/10.1029/2000jb900041>
- 462 Harmon, N., Forsyth, D. W., Lamm, R., & Webb, S. C. (2007). Pand Swave delays beneath  
463 intraplate volcanic ridges and gravity lineations near the East Pacific Rise. *Journal of*  
464 *Geophysical Research-Solid Earth and Planets*, 112(B3), 1961–12.  
465 <https://doi.org/10.1029/2006jb004392>
- 466 Haxby, W. F., & Weissel, J. K. (1986). Evidence for small-scale mantle convection from Seasat  
467 altimeter data. *Journal of Geophysical Research*, 91(B3), 3507–3520.  
468 <https://doi.org/10.1029/jb091ib03p03507>
- 469 Hirschmann, M. M. (2010). Partial melt in the oceanic low velocity zone. *Physics Of The Earth*  
470 *And Planetary Interiors*, 179(1–2), 60–71. <https://doi.org/10.1016/j.pepi.2009.12.003>
- 471 Holmes, R. C., Webb, S. C., & Forsyth, D. W. (2007). Crustal structure beneath the gravity  
472 lineations in the Gravity Lineations, Intraplate Melting, Petrologic and Seismic Expedition  
473 (GLIMPSE) study area from seismic refraction data. *Journal of Geophysical Research*,  
474 112(B7), B07316. <https://doi.org/10.1029/2006JB004685>
- 475 Holtzman, B. K. (2016). Questions on the existence, persistence, and mechanical effects of a  
476 very small melt fraction in the asthenosphere. *Geochemistry Geophysics Geosystems*, 17, 470–  
477 484. <https://doi.org/10.1002/2015gc006102/pdf>

- 478 Incorporated Research Institutions for Seismology. (2015). Data Services Products: Syngine.  
479 <https://doi.org/10.17611/DP/SYNGINE.1>
- 480 Jackson, I., & Faul, U. H. (2010). Grainsize-sensitive viscoelastic relaxation in olivine: Towards  
481 a robust laboratory-based model for seismological application. *Physics Of The Earth And*  
482 *Planetary Interiors*, 183(1–2), 151–163. <https://doi.org/10.1016/j.pepi.2010.09.005>
- 483 Karato, S., & Jung, H. (1998). Water, partial melting and the origin of the seismic low velocity  
484 and high attenuation zone in the upper mantle. *Earth and Planetary Science Letters*, 157(3–4),  
485 193–207.
- 486 Kawakatsu, H., Kumar, P., Takei, Y., Shinohara, M., Kanazawa, T., Araki, E., & Suyehiro, K.  
487 (2009). Seismic evidence for sharp lithosphere-asthenosphere boundaries of oceanic plates.  
488 *Science*, 324(5926), 499–502. <https://doi.org/10.1126/science.1169499>
- 489 Kennet, B., & Engdahl, E. R. (1991). Traveltimes for global earthquake location and phase  
490 identification. *Geophysics Journal International*, 105, 429–465.
- 491 Lin, P., Gaherty, J. B., Jin, G., Collins, J. A., & Lizarralde, D. (2016). High-resolution seismic  
492 constraints on flow dynamics in the oceanic asthenosphere. *Nature*, 535, 438–541.
- 493 Ma, Z., Dalton, C. A., Russell, J. B., Gaherty, J. B., Hirth, G., & Forsyth, D. W. (2020). Shear  
494 attenuation and anelastic mechanisms in the central Pacific upper mantle. *Earth and Planetary*  
495 *Science Letters*, 536, 116148. <https://doi.org/10.1016/j.epsl.2020.116148>
- 496 Manjón-Cabeza Córdoba, A., & Ballmer, M. D. (2021). The role of edge-driven convection in  
497 the generation of volcanism – Part 1: A 2D systematic study. *Solid Earth*, 12(3), 613–632.  
498 <https://doi.org/10.5194/se-12-613-2021>

- 499 Parsons, B., & Sclater, J. G. (1977). An analysis of the variation of ocean floor bathymetry and  
500 heat flow with age. *Journal of Geophysical Research*, 82(5). Retrieved from  
501 <http://www.agu.org/pubs/crossref/1977/JB082i005p00803.shtml>
- 502 Parsons, Barry, & McKenzie, D. (1978). Mantle convection and the thermal structure of the  
503 plates. *Journal of Geophysical Research*, 83(B9), 4485.  
504 <https://doi.org/10.1029/JB083iB09p04485>
- 505 Richter, F. M., & Parsons, B. (1975). On the interaction of two scales of convection in the  
506 mantle. *Journal of Geophysical Research*. <https://doi.org/10.1029/jb080i017p02529/pdf>
- 507 Russell, J., Gaherty, J. B., Eilon, Z. C., Forsyth, D. W., & Ekström, G. (2021). Heterogeneous  
508 Mantle Flow and Deviations from Half-Space Cooling Observed Beneath the Central Pacific.  
509 Presented at the AGU Fall Meeting 2021, New Orleans, LA, USA, DI15C-0033.
- 510 Russell, J. B. (2021). *Structure and Evolution of the Oceanic Lithosphere-Asthenosphere System*  
511 *from High-Resolution Surface-Wave Imaging* (PhD Thesis). *ProQuest Dissertations and*  
512 *Theses*. Retrieved from [https://www.proquest.com/dissertations-theses/structure-evolution-](https://www.proquest.com/dissertations-theses/structure-evolution-oceanic-lithosphere/docview/2492599842/se-2?accountid=14522)  
513 [oceanic-lithosphere/docview/2492599842/se-2?accountid=14522](https://www.proquest.com/dissertations-theses/structure-evolution-oceanic-lithosphere/docview/2492599842/se-2?accountid=14522)
- 514 Russell, J. B., Gaherty, J. B., Lin, P.-Y. P., Lizarralde, D., Collins, J. A., Hirth, G., & Evans, R.  
515 L. (2019). High-Resolution Constraints on Pacific Upper Mantle Petrofabric Inferred From  
516 Surface-Wave Anisotropy. *Journal of Geophysical Research*, 35(3), 415–27.  
517 <https://doi.org/10.1029/2018jb016598>
- 518 Sandwell, D., & Fialko, Y. (2004). Warping and cracking of the Pacific plate by thermal  
519 contraction. *Journal of Geophysical Research*, 109(B10).  
520 <https://doi.org/10.1029/2004jb003091>

- 521 Sandwell, D. T., Winterer, E. L., Mammerickx, J., Duncan, R. A., Lynch, M. A., Levitt, D. A., &  
522 Johnson, C. L. (1995). Evidence for diffuse extension of the Pacific Plate from Pukapuka  
523 ridges and cross-grain gravity lineations. *Journal of Geophysical Research: Solid Earth*,  
524 *100*(B8), 15087–15099. <https://doi.org/10.1029/95JB00156>
- 525 Schmandt, B., & Humphreys, E. (2010). Seismic heterogeneity and small-scale convection in the  
526 southern California upper mantle. *Geochemistry Geophysics Geosystems*, *11*(5), Q05004.  
527 <https://doi.org/10.1029/2010gc003042>
- 528 Schmerr, N. (2012). The gutenbergs discontinuity: Melt at the lithosphere-asthenosphere  
529 boundary. *Science*, *335*(6075), 1480–1483. <https://doi.org/10.1126/science.1215433>
- 530 Smith, W. H. F., & Sandwell, D. T. (1997). Global Sea Floor Topography from Satellite  
531 Altimetry and Ship Depth Soundings. *Science*, *277*(5334), 1956–1962.  
532 <https://doi.org/10.1126/science.277.5334.1956>
- 533 Stein, C. A., & Stein, S. (1992). A model for the global variation in oceanic depth and heat flow  
534 with lithospheric age. *Nature*, *359*(6391), 123–129. <https://doi.org/10.1038/359123a0>
- 535 Stern, T. A., Henrys, S. A., Okaya, D., Louie, J. N., Savage, M. K., Lamb, S., et al. (2015). A  
536 seismic reflection image for the base of a tectonic plate. *Nature*, *518*(7537), 85–88.  
537 <https://doi.org/10.1038/nature14146>
- 538 Takei, Y., & Holtzman, B. K. (2009). Viscous constitutive relations of solid-liquid composites in  
539 terms of grain boundary contiguity: 1. Grain boundary diffusion control model. *Journal of*  
540 *Geophysical Research-Solid Earth and Planets*, *114*(B6), B06205.  
541 <https://doi.org/10.1029/2008jb005850>

- 542 Tharimena, S., Rychert, C., Harmon, N., & White, P. (2017). Imaging Pacific lithosphere seismic  
543 discontinuities—Insights from SS precursor modeling. *Journal of Geophysical Research: Solid*  
544 *Earth*, *122*(3), 2131–2152. <https://doi.org/10.1002/2016JB013526>
- 545 VanDecar, J. C., & Crosson, R. S. (1990). Determination of teleseismic relative phase arrival  
546 times using multi-channel cross-correlation and least squares. *Bulletin of the Seismological*  
547 *Society of America*, *80*(1), 150–169.
- 548 Weeraratne, D. S., Forsyth, D. W., Yang, Y., & Webb, S. C. (2007). Rayleigh wave tomography  
549 beneath intraplate volcanic ridges in the South Pacific. *Journal of Geophysical Research-Solid*  
550 *Earth and Planets*, *112*(B6), B06303. <https://doi.org/10.1029/2006jb004403>
- 551 Yamauchi, H., & Takei, Y. (2020). Application of a Premelting Model to the Lithosphere-  
552 Asthenosphere Boundary. *Geochemistry, Geophysics, Geosystems*, *21*(11).  
553 <https://doi.org/10.1029/2020GC009338>
- 554 Zelt, C. A. (1998). Lateral velocity resolution from three-dimensional seismic refraction data.  
555 *Geophysical Journal International*, *135*(3), 1101–1112.

556